Electrochimica Acta 179 (2015) 565–577

Contents lists available at ScienceDirect

Electrochimica Acta

journal homepage: www.elsevier.com/locate/electacta

Syngas (CO-H_2) production using high temperature micro-tubular solid oxide electrolysers

L. Kleiminger, T. Li, K. Li, G.H. Kelsall*

Department of Chemical Engineering, Imperial College London, London SW7 2AZ, UK

ARTICLE INFO

Article history:
Received 22 January 2015
Received in revised form 9 July 2015
Accepted 10 July 2015
Available online 26 July 2015

Keywords:
solid oxide electrolyser
micro-tubular
CO_2/H_2O reduction
(reverse) water gas shift reaction
oxygen-18 isotopic labelling

ABSTRACT

CO_2 and/or H_2O were reduced to CO/H_2 in micro-tubular solid oxide electrolysers with yttria-stabilized zirconia (YSZ) electrolyte, Ni-YSZ cermet cathode and strontium(II)-doped lanthanum manganite (LSM) oxygen-evolving anode. At 822 °C, the kinetics of CO_2 reduction were slower (ca. $-0.49\,A\,cm^{-2}$ at 1.8 V) than H_2O reduction or co-reduction of CO_2 and H_2O, which were comparable (ca. -0.83 to $-0.77\,A\,cm^{-2}$ at 1.8 V). Performances were improved (-0.85 and $-1.1\,A\,cm^{-2}$ for CO_2 and H_2O electrolysis, respectively) by substituting the silver current collector with nickel and avoiding blockage of entrances to pores on the inner lumen of micro-tubes induced by silver paste applied previously to decrease contact losses. The change in current collector materials increased ohmic potential losses due to substituting the lower resistance Ag with Ni wire, but decreased electrode polarization losses by 80–93%. For co-electrolysis of CO_2 and H_2O, isotopically-labelled $C^{18}O_2$ was used to try to distinguish between direct cathodic reduction of CO_2 and its Ni-catalysed chemical reaction with hydrogen from reduction of steam. Unfortunately, oxygen was exchanged between $C^{18}O_2$ and $H_2{}^{16}O$, enriching oxygen-18 in the steam and substituting oxygen-16 in the carbon dioxide, so the anode off-gas isotopic fractions were meaningless. This occurred even in alumina and YSZ tubes without the micro-tubular reactor, i.e. in the absence of Ni catalyst, though not in quartz tubes. Unfortunately, larger differences between the thermal expansion coefficients of quartz and YSZ precluded using a quartz tube to house the micro-tubular reactor. However, the kinetic results, CO/H_2 yields from off-gas analysis, diffusional considerations and model predictions of reactant and product gas adsorption on Ni suggested that syngas should be produced by electrochemical reduction of steam to H_2, followed by its Ni-catalysed chemical reaction with CO_2.

1. Introduction

As contributions of renewable energy to electricity grids increase, large-scale energy storage becomes more important, because of the intermittency of renewables and the dynamics of power demand arising from social habits causing misalignments, precluding supply-demand balancing. Two different time scales have to be addressed: (1) daily fluctuations and (2) seasonal fluctuations. Therefore, storing electrical energy in chemical bonds using electrolysis of H_2O and/or CO_2 to balance supply and demand could be a promising technology, as infrastructure to store chemicals (e.g. methane in gas grids) is already available. Furthermore, smoothing geographical variations could also be more facile.

Solid oxide electrolysers offer the advantage of fuel flexibility [1,2] in addition to thermodynamic and kinetic benefits of operating at temperatures >700 °C, meaning a larger proportion of electrical energy can be substituted by thermal energy [3] (Fig. 1). The proposed reaction scheme is outlined in reactions (1)–(4) for co-electrolysis of CO_2 and H_2O to produce syngas:

$$\text{Fuel electrode (e.g. Ni)}: CO_2 + 2e^- \rightarrow CO + O^{2-} \tag{1}$$

$$\nu\left(H_2O + 2e^- \rightarrow H_2 + O^{2-}\right) \tag{1b}$$

$$\text{Electrolyte (e.g. YSZ)}: O^{2-}(\text{cathode}) \rightarrow O^{2-}(\text{anode}) \tag{2}$$

$$\text{Air electrode (e.g. LSM)}: \frac{1+\nu}{2}\left(2O^{2-} \rightarrow O_2 + 4e^-\right) \tag{3}$$

$$\text{Overall}: CO_2 + \nu H_2O \rightarrow CO + \nu H + \frac{1+\nu}{2}O_2 \tag{4}$$

Electrolysis of CO_2 on its own has the disadvantage that carbon formation via the Boudouard reaction (5) is possible, if the CO concentration is too high and temperatures too low [6]; carbon

---

* Corresponding author. Tel.: +44 (0)20 7594 5633.
E-mail address: g.kelsall@imperial.ac.uk (G.H. Kelsall).

http://dx.doi.org/10.1016/j.electacta.2015.07.062

Nomenclature

A_i	Arrhenius parameters for the desorption reaction rate constant for reaction i (mol, m, s)
a_i	Sticking coefficient parameter for reaction i
c_k	Molar concentration of gaseous species k (mol m^{-3})
$c_{surf,k}$	Surface concentration of species k (mol m^{-2})
b_i	Sticking coefficient parameter for reaction i
$C_{Nisites}$	Surface molar concentration of nickel sites (mol m^{-2})
$D_{i\text{-}j}$	Binary diffusion coefficient (m^2 s^{-1})
D_{ik}	Knudsen diffusion coefficient of species i (m^2 s^{-1})
d_i	Sticking coefficient parameter for reaction i (kJ mol^{-1})
d_m	Molecular diameter (pm)
dn/dt	change in reactant-product (e.g. CO_2-CO) (mol s^{-1})
d_{pore}	Pore diameter (m)
E_a	Activation energy (kJ mol^{-1})
ΔE	Equilibrium potential (V)
F	Faraday constant (96,485) (C mol^{-1})
F	Frequency (Hz)
I	Total current (A)
K_O	Knudsen flow parameter (m)
K_s	Surface species excluding nickel bare sites
K_T	Equilibrium constant at temperature T
$k_{a,i}$	Rate coefficient for adsorption reaction i (m, mol, s)
$k_{d,i}$	Rate coefficient for desorption reaction i (m, mol, s)
M	Molecular weight (g mol^{-1})
N_A	Avogadro constant (6.0221×10^{23}) (mol^{-1})
P	Pressure (Pa)
p_x	Partial pressures (of CO_2, CO, O_2) (Pa)
R	Universal gas constant (8.3145) (J mol^{-1} K^{-1})
S_i^0	Initial sticking coefficient
T	Temperature (K)
ν	Stoichiometric coefficient
Z	Area-specific impedance (Ω cm^2)
x_i	Species i mole fraction
Γ	Surface site density (mol m^{-2})
β_i	Arrhenius parameters for the desorption reaction rate constant of reaction i
ε_{ik}	Activation energy dependence on species k and reaction i (kJ mol^{-1})
θ_k	Fractional surface coverage of species k
λ_m	Mean free path length (m)
ν_e	Electron stoichiometry of reaction
σ_k	Site occupancy number

could also be formed by CO reduction. Hence, co-electrolysis is beneficial to produce syngas, because water has been reported to suppress carbon formation [3] and syngas can be used as the feedstock, e.g. in the Fischer-Tropsch process to produce synthetic liquid fuels [7] or direct methanation by the Sabatier reaction downstream of the electrolytically active zone [8]. However, the syngas composition achieved by the electrochemical processes can be altered by the (reverse) water gas shift reaction (6), which would limit the tunability of the syngas production.

$$2CO \rightleftarrows C + CO_2 \tag{5}$$

$$CO_2 + H_2 \underset{\text{water gasshift reaction}}{\overset{\text{reverse water gas shift reaction}}{\rightleftarrows}} H_2O + CO \tag{6}$$

Co-electrolysis has been studied on various cathode materials including LSCM (lanthanum strontium chromium manganite)/GDC (gadolinium doped ceria) [9], Ni-GDC, Ni/Ru-GDC [10] and conventional Ni-YSZ (yttria-stabilized zirconia) [3,11,12] cermets, all of which exhibited the highest performance for steam electrolysis, with co-electrolysis performing nearly identically, and CO_2 electrolysis performance being the worst. In fuel cell mode, oxidation of H_2 compared to CO was found to be 1.9-3.1 times faster, whereas CO oxidation by the water gas shift reaction was shown to be much faster than the electrochemical processes [13]. Therefore, it is likely that CO is produced in co-electrolysis mainly via the reverse water gas shift reaction, whereas the electrochemical processes are dominated by water electrolysis, so explaining the similar behaviour between H_2O and co-electrolysis [6,11,14]. Ebbensen et al. [15] reported that electrochemical reduction of both H_2O and CO_2 occurred within their solid oxide electrolyser, though in parallel with the (reverse) water gas shift reaction [12] due to its fast kinetics; this was supported by recently reported results of computational modelling [16] of the direct and indirect (i.e. via electrogenerated H_2) reduction of CO_2. The direction of the water gas shift reaction could be forward or backwards depending on the operating conditions ($K_T = 1$ at 838 °C), implying that at high temperatures, CO was being produced electrochemically and shifted by reaction (6) towards producing H_2.

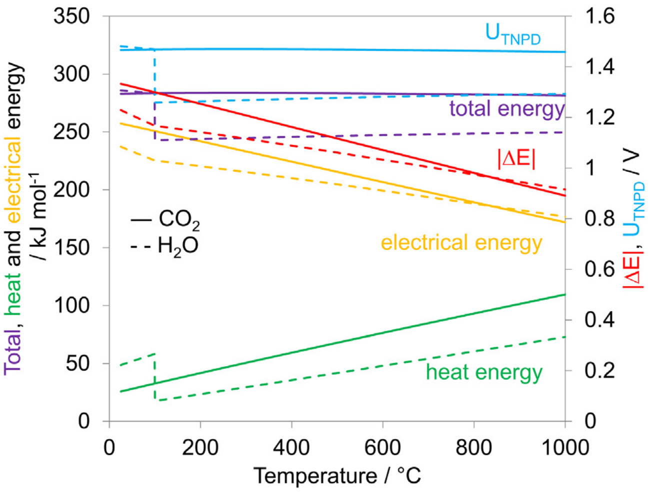

Fig. 1. Thermodynamics of H_2O (- -) compared to CO_2 (__) electrolysis (calculated with thermodynamic data from Chase [4] and Herrington [5]); |ΔE| and U_{TNPD} are equilibrium and thermo-neutral potential differences, respectively.

Results are reported below for CO_2 and/or H_2O reduction to CO/H_2 in micro-tubular solid oxide electrolysers (MT-SOE) with yttria-stabilized zirconia (YSZ) electrolyte, Ni-YSZ cermet cathode and strontium-doped lanthanum manganite (LSM) oxygen-evolving anode. This is the first report of co-electrolysis of CO_2 and H_2O in a micro-tubular (<1.5 mm outer diameter) solid oxide electrolyser, together with effects of coupling their direct electrochemical reduction to the reverse water gas shift reaction (i.e. indirect CO_2 reduction by electrogenerated hydrogen) within the cathode structure. Co-electrolysis has been mentioned in tubular SOEs previously [8,11], but these tubes were of larger size (4.5–9.8 mm outer diameter). The micro-tubular design reported here has the advantage of 3–6 times higher volumetric current density, as well as higher volumetric density of catalyst area for the syngas reaction. Furthermore, the paper by Chen et al. [8] (4.5 mm outer diameter reactor size) lacks critical information about reactor design such as current collection, which has been identified as a major factor of reactor performance, as discussed below.

The objectives were to correlate electrolyser performance with reactant gas composition and current collector material(s). Insight

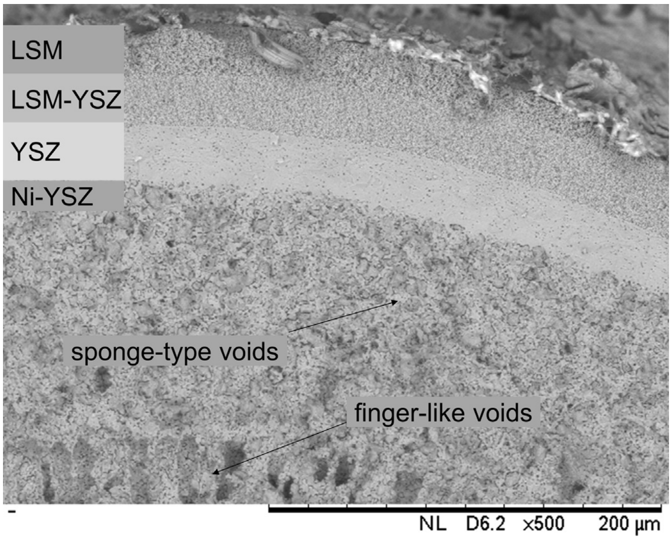

Fig. 2. Scanning electron micrograph of Ni-YSZ|YSZ|LSM-YSZ|LSM micro-tubular reactor.

into the role of the water gas shift reaction in co-electrolysis will be discussed based on the electrochemical performance, electrical impedance, gas diffusion considerations in conjunction with microstructure, off-gas composition, adsorption modelling and electrolysis of isotopically-labelled reactant gases.

2. Experimental

The micro-tubular reactors were fabricated by a dual-layer co-extrusion phase inversion technique to produce electrode | electrolyte hollow fibres, which after co-sintering were brush-coated with the outer anode layers [17]. The individual layers (Fig. 2) were a NiO – $(ZrO_2)_{0.92}(Y_2O_3)_{0.08}$ (YSZ) cathode | YSZ electrolyte | $La_{0.8}Sr_{0.2}MnO_{3-\delta}$ (LSM) – YSZ anode | LSM current collection layer; NiO was activated by reduction to elemental nickel in a hydrogen atmosphere. The thicknesses of the individual layers were: ca. 230 μm Ni-YSZ | 26 μm YSZ | 25 μm LSM-YSZ | 25 μm LSM, with an active length of the outer anode of 15 mm.

The cells were previously analysed for gas tightness, mechanical strength, material homogeneity (using energy dispersive spectroscopy), porosity and pore size distribution. Details of the measurement techniques and results can be found elsewhere [17].

2.1. Scanning electron microscopy and energy dispersive spectroscopy

Microstructures of the micro-tubular solid oxide reactors were imaged using scanning electron microscopy (SEM). The exact dimensions of each fibre post-testing were confirmed using Hitachi table-top scanning electron microscopes (TM-1000 and TM3030) at 15 kV accelerating voltage. Energy dispersive spectroscopy (EDS) was performed at 20 kV on a JEOL instrument (JSM 6400).

2.2. Electrochemical Characterisation

2.2.1. Current collection, sealing and reactor assembly

Current collection on the Ni-YSZ inner electrode was achieved via two designs. Design one used twisted 0.25 mm diameter silver wires (99.9% purity, annealed, VWR International LLC, UK), wrapped with silver wool (99.9% purity, VWR International LLC, UK) fed through the inner lumen of the hollow fibre. The contact between wires/wool and the inner surface was enhanced by conductive silver paste (VWR International LLC, UK). The second design option was a tight coiled 0.25 diameter nickel wire (99.9% purity, Sigma Aldrich, UK) pulled through the inner lumen. The nickel wire was connected to silver wires (0.25 mm diameter) such that the latter could be connected outside of the reducing atmosphere without risk of oxidation. For the outer LSM electrodes, silver wires of 0.2 mm diameter (99.99%, annealed, Advent Research Materials, UK) were wrapped around the hollow fibre and fixed with silver paste. The length of individual wires from fibre to electrical connections was ca. 400 mm. The hollow fibre reactor was then cemented into an alumina tube (to feed the cathode gases) and the entire assembly sealed into a quartz tube with stainless steel end-caps as described previously [17].

2.2.2. Electrolyser Performance Tests

To generate steam, a controlled evaporation unit was used (CEM-unit, Bronkhorst, UK), in which water was mixed and heated with the feed gases to produce vapour at a controlled rate. However, the design of the system required a carrier gas flowing at $\geq$50 ml min^{-1}, so the active gas fraction (H_2O, H_2, CO_2, CO) was only 44% during electrolysis operation. All gases or liquid (water) flow rates were controlled by automated mass-flow controllers (Bronkhorst, UK); the individual feed gas scenarios are outlined in Table 1. For the oxygen-18 isotopically labelled co-electrolysis, 95.5% enriched $C^{18}O_2$ was used (99.9% chemical purity, Isotec, Sigma Aldrich, UK) and individual cathodic feed gas compositions are outlined in the respective results section; the total flow of 90 ml min^{-1} with 50 ml min^{-1} carrier gas was kept constant and the anodic feed gas composition corresponded to the 'standard' ($C^{16}O_2$) electrolysis scenarios.

The reactor was heated in a tubular furnace (Elite Thermal Systems Ltd., UK) to 650 °C and the nickel oxide reduced to nickel with hydrogen for 2 hours. After reduction, the temperature was increased to the operating temperatures (768, 822 and 872 °C), monitored by a N-type thermocouple. The silver wires were connected to a potentiostat/galvanostat equipped with a frequency

Table 1
Feed gas composition scenarios to the cathode (Ni-YSZ inner electrode).

	$CO_{(g)}$	$CO_{2(g)}$	$H_{2(g)}$	Cathode (Ni-YSZ)[1] $H_2O_{(l)}$ (ml hr^{-1} liquid feed before evaporation)/ ml min^{-1}gas volume	$He_{(g)}$	Total	Anode (LSM-YSZ|LSM) 10% O_2 in Argon/ ml min^{-1}
Heat-up					50	50	62
Reduction			16		50	66	62
Scenario 1: 'CO2 electrolysis'	8	32	–	–	50	90	90
Scenario 2: 'H_2O electrolysis'	–	–	8	32 (1.392)	50	90	90
Scenario 3: 'co-electrolysis'	4	16	4	16 (0.696)	50	90	90

[1] CO or H_2 were co-fed to the electrolyser to prevent re-oxidation of the nickel at open-circuit potential difference.

response analyser (FRA) 4.9 module for electrochemical impedance measurements (PGSTAT302N, Metrohm Autolab B.V., Netherlands). Electrochemical test procedures for operation were created in Nova 1.10.2 software (Metrohm Autolab B.V., Netherlands).

The electrochemical experiments included measuring the potential difference response of the cell to linearly scanned applied current and steady state measurements over varying time scales at constant potential difference or constant current. The intrinsic electrical properties of materials and interfaces were characterized using electrochemical impedance spectroscopic (EIS) measurements at open circuit potential difference (U_{OCPD}) and operating potential differences in the frequency range of 10^5–0.1 Hz (with an RMS amplitude of 0.01 V for constant potential difference operation.)

On-line analysis of the cathode (Ni-YSZ) off-gases was performed using mass spectrometry (Genesys 200D, ESS Ltd, UK) monitoring the reactant consumption/product formation, as well as detecting radial leakage across imperfections in the hollow fibres. A second optional mass spectrometer was used to detect the anodic (LSM-YSZ|YSZ) off-gases during experiments with $C^{18}O_2$ fed to the cathode. The water within the reactor was condensed in a quartz U-bend immersed in ice-water to avoid flooding of the mass spectrometer. A schematic of the equipment is outlined in Fig. 3.

3. Results and Discussion

3.1. Characterization of hollow fibre reactors

Finger-like voids extended into the cathode layer to a depth corresponding to 44% of its thickness, with the remaining part of the cathode being of a sponge-type nature with a mean porosity >30% after reduction. The mechanical strength was 156 (±26) MPa and the gas tightness 2.56×10^{-10} mol m^{-2} s^{-1} Pa^{-1}, both values being comparable to values reported in the literature [18,19].

3.2. Reactor performance

3.2.1. Electrochemical performance of the MT-SOEs

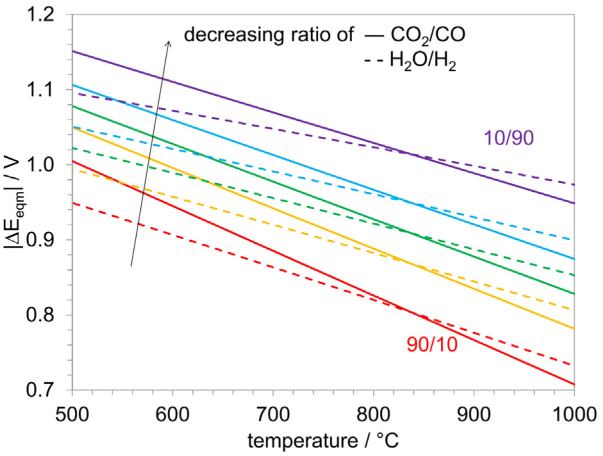

Fig. 4. Effect of operating temperature on theoretical equilibrium potential differences for different CO_2/CO (—) and H_2O/H_2 (- -) ratios.

The theoretical open circuit potential differences for pure H_2O or CO_2 electrolysis are plotted in Fig. 4, using the Nernst equation (7a) and (7b). The measured values were generally in good agreement with their predicted values, implying gas-tight electrolytes.

$$\Delta E = \Delta E^{\circ}_{CO_2/CO,T} + \frac{RT}{2F}\ln\left[\frac{p_{CO_2}}{p_{CO}\sqrt{p_{O_2}}}\right] \quad (7a)$$

or

$$\Delta E = \Delta E^{\circ}_{H_2O/H_2,T} + \frac{RT}{2F}\ln\left[\frac{p_{H_2O}}{p_{H_2}\sqrt{p_{O_2}}}\right] \quad (7b)$$

Fig. 5(A) shows the effect of current density, cathode feed gas composition and inner electrode current collector design on cell potential difference at a fixed electrolyte thickness. Corresponding electrochemical impedance spectra are shown in Fig. 5(B) and summarized in Table 2. For all cases, H_2O electrolysis outperformed pure CO_2 electrolysis, whereas the co-electrolysis

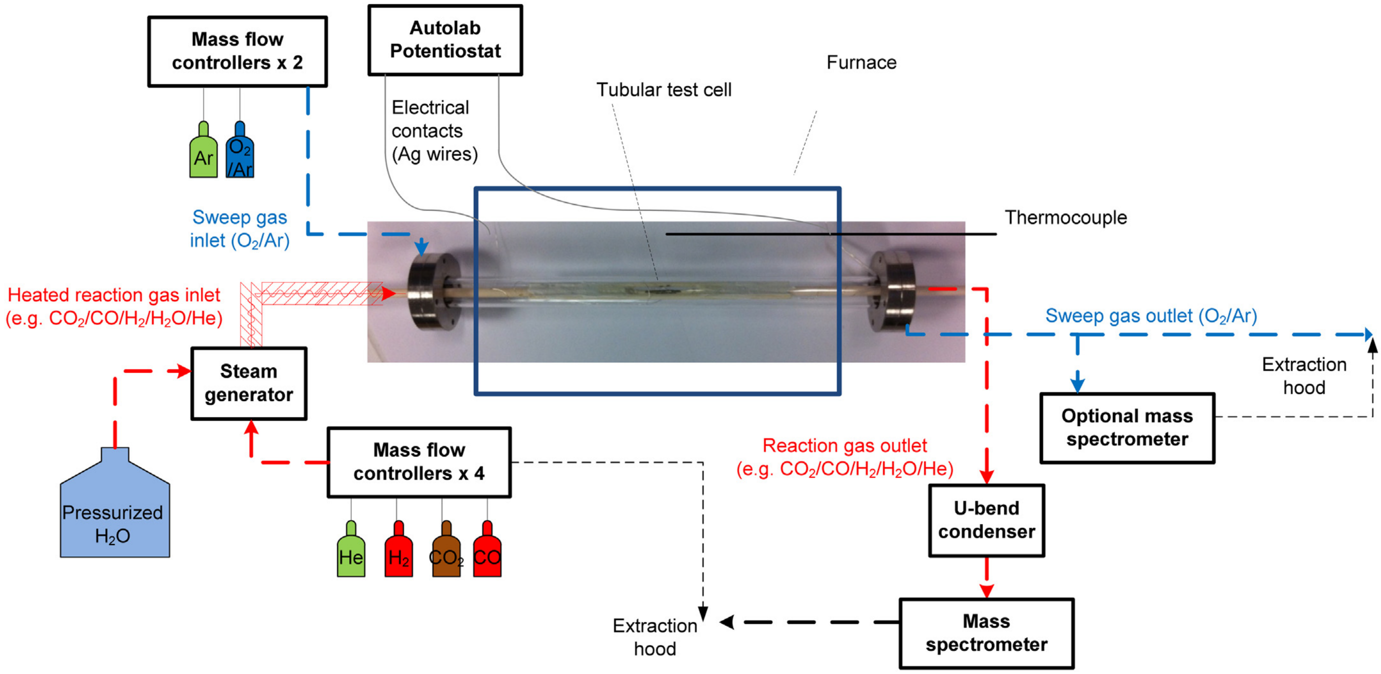

Fig. 3. Schematic of experimental system.

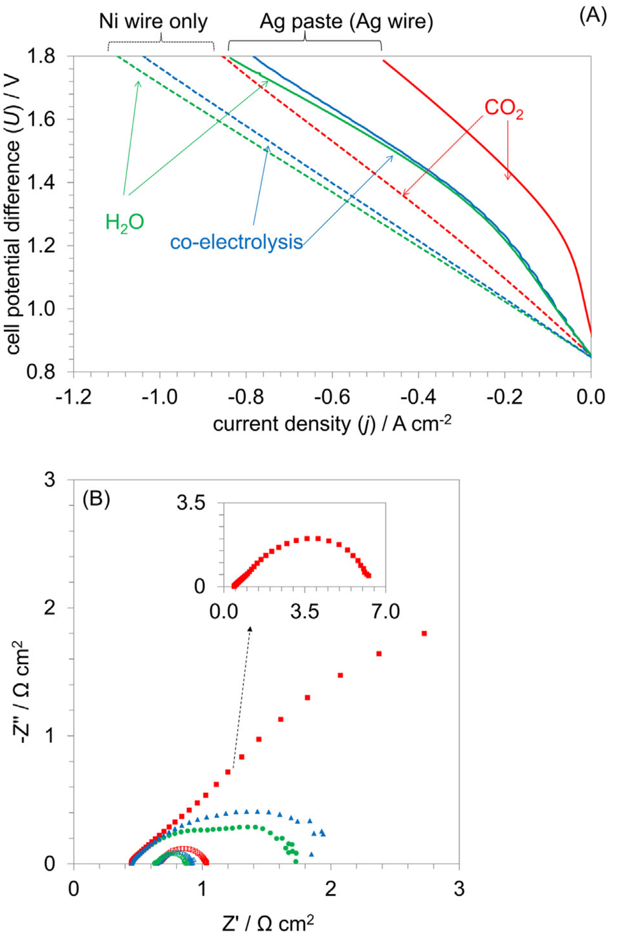

Fig. 5. (A) Effects of applied current density (*j*) and current collection technique (- - - Ni wire alone, —Ag wire + Ag paste) on cell potential difference (*U*) at 822 °C for H_2O, CO_2 and co-electrolysis with gas feed composition outlined in Table 1. (B) Impedance spectra for the same scenarios, measured at U_{OCPD} with CO_2 (■), H_2O (●) and co-electrolysis (▲), filled (Ag wire + Ag paste) and unfilled (Ni wire alone).

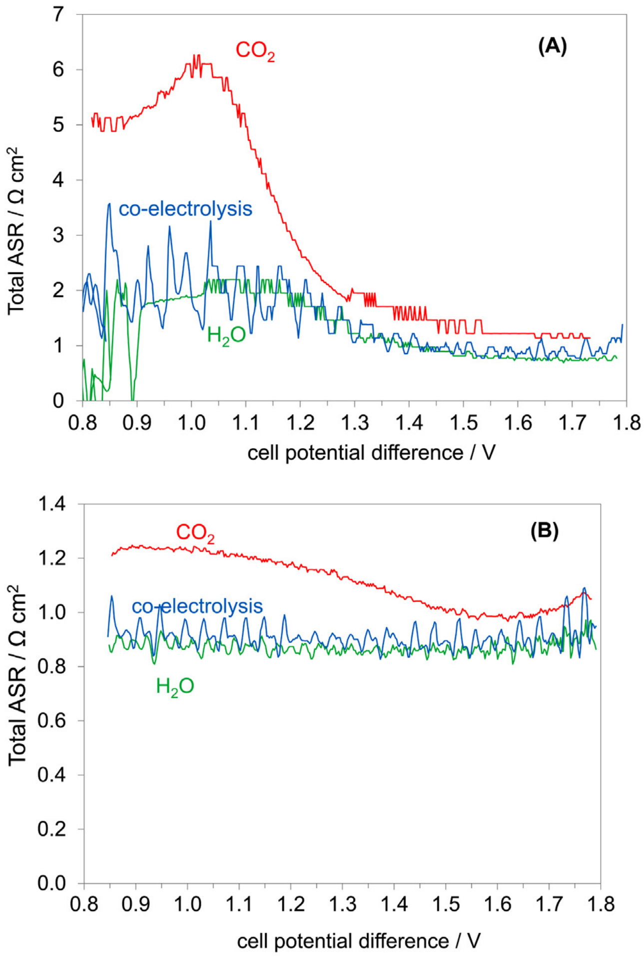

Fig. 6. Effect of cell potential difference on total area specific resistance at 822 °C for (A) silver paste plus silver wire and (B) nickel wire.

behaviour was usually close to that of H_2O electrolysis. The performance variation for the different feed gas scenarios was related only to electrode polarization, with the ohmic resistance being unaffected by the nature of the feed gas.

The variation in ohmic resistance for different current collector designs, i.e. lower ohmic area specific resistance for silver wire plus silver paste[1,2] compared to nickel wire only, was due to the higher electronic conductivity of silver [20] ($1.4 \times 10^7\,S\,m^{-1}$ at 1073 K) compared to that of nickel [21] ($2.1 \times 10^6\,S\,m^{-1}$ at 1073 K). For a detailed discussion about different current collector design options investigated for CO_2 electrolysis alone, the reader is referred to [22], which also discusses the negative effect of silver paste on electrode polarization for the case of electrolysis of CO_2 alone.

Notably, the difference in the apparent kinetics between H_2O and CO_2 electrolysis also depended on the cathode current collection design. For the silver wire plus paste option, electrode polarization was 380 % higher for CO_2 electrolysis compared to that for H_2O electrolysis. Contrastingly, for the nickel wire alone electrode polarization was only 61% higher for CO_2 compared to H_2O splitting (at U_{OCPD}), so CO_2 electrolysis was affected more by the silver paste than was H_2O electrolysis.

Fig. 6(A) and (B) shows that this difference between the behaviour of CO_2 and H_2O electrolysis varied with applied cell potential difference. However, even at an applied cell potential difference of e.g. 1.5 V, 16% and 64% difference in overall performance between CO_2 and H_2O electrolysis were measured for nickel wire only and silver wire plus silver paste current collector, respectively.

The current densities achieved of $-0.5\,A\,cm^{-2}$ at 1.3 V with 35% humidity at 822 °C (steam electrolysis – feed gas scenario 2) were comparable with those of (micro)-tubular reactors reported elsewhere [11,23] ranging between ca. $-0.4\,A\,cm^{-2}$ (850 °C, 25%

Table 2
Contributions to area specific resistances (ASR) for different feed gas compositions and current collection techniques at 822 °C.

		Ohmic ASR/Ω cm^2	Electrode ASR/Ω cm^2	Total ASR/Ω cm^2
Ag wire + Ag paste	Scenario 1 (CO_2)	0.448	6.15	6.60
	Scenario 2 (H_2O)	0.453	1.28	1.73
	Scenario 3 (CO_2/H_2O)	0.453	1.55	2.00
Ni wire only	Scenario 1 (CO_2)	0.644	0.406	1.05
	Scenario 2 (H_2O)	0.629	0.251	0.880
	Scenario 3 (CO_2/H_2O)	0.640	0.284	0.924

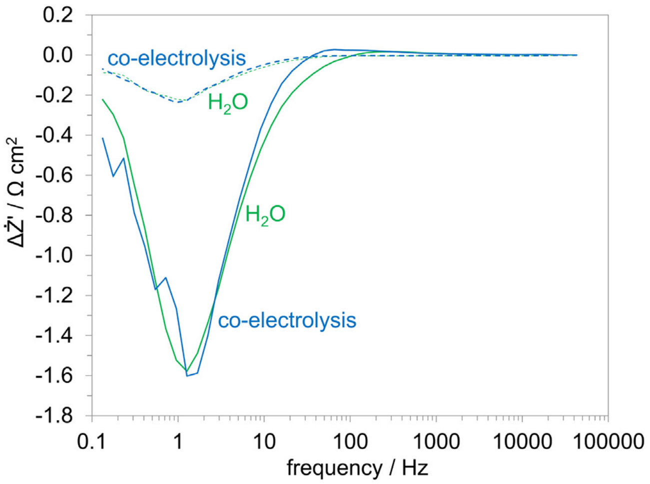

Fig. 7. Effects of gas composition and lumen current collector material (- - Ni wire only, —Ag wire + Ag paste) on $\Delta\dot{Z}'$ at U_{OCPD} with CO_2 electrolysis as the reference point at 822 °C.

steam) to ca. $-0.7\,A\,cm^{-2}$ (900 °C, 30% steam), though the latter electrolyte thicknesses were thinner at only 20–15 μm.

3.2.2. Why was CO_2 electrolysis more affected by current collector design?

Using analysis in differences of impedance spectra (8), as shown in Fig. 7, the variations between CO_2 and H_2O/co-electrolysis were determined to be all due to low frequency resistances, which can be attributed to differences in gas diffusion rates [3,24]. The magnitude of changes was determined by the cathode lumen current collector design, with a large variation detected for the Ag paste-containing cells.

$$\Delta\dot{Z}'(f_n) \cong \frac{[Z'_{gas1}(f_{n+1}) - Z'_{gas1}(f_{n-1})] - [Z'_{gas2}(f_{n+1}) - Z'_{gas2}(f_{n-1})]}{\ln\left(\frac{f_{n+1}}{f_{n-1}}\right)} \qquad (8)$$

The application of conductive silver paste on the lumen surface was the only difference between the reactors, so most probably it increased gas diffusional transport resistances into the cathode microstructure (Fig. 8) by partial blockage of the entrances to surface pores. Energy dispersive spectroscopic analysis (Fig. 9) confirmed that silver was confined to the inner surface of the hollow fibre reactor, rather than within the Ni-YSZ scaffold.

Being a lighter and smaller [25] (265 versus 330 pm) molecule than CO_2, water could diffuse more easily into the structure. Table 3 lists the binary diffusion coefficients, calculated according to the procedure by Fuller et al. [26], for the different feed gases relative to the helium carrier gas, with molecular diffusion rates of steam being predicted to be ca. 1.5 greater than for CO_2.

However, silver paste probably caused partial blockage of the entrances to pores in the cathode, effectively decreasing the effective pore size. For smaller pores, molecule-wall interactions are more likely; hence, Knudsen diffusion would be more appropriate (9). The mean free path for the five gas species are ca. 510, 310, 240, 490, 410 nm for He, CO_2, CO, H_2O and H_2, respectively, calculated according to Eq. (10) using kinetic molecular diameters [25,27]. The mean peak pore sizes in 'unblocked' reduced hollow fibres were measured to be ca. 17, 400 and 700 nm using mercury porosimetry. Thus, the mean free paths of the reactants and products were of similar size to the pore sizes, so Knudsen diffusion was relevant.

Table 4 lists the diffusion coefficients for 400 and 700 nm pore sizes (approximating K_0 to $0.25 \times d_{pore}$); the ratio of the diffusion coefficients compared to water would be: 3, 0.64, 0.80 for H_2, CO_2 and CO, respectively, again CO_2 being the slowest to diffuse.

$$D_{i,k} = \frac{4}{3}K_0\sqrt{\frac{8RT}{\pi M_i}} \sim \sqrt{\frac{1}{M_i}} \qquad (9)$$

$$\lambda_m = \frac{RT}{\sqrt{2}\pi d_{m,i}^2 N_A P} \qquad (10)$$

3.2.3. Implication of performance differences of CO_2 and H_2 for their co-electrolysis

The electrochemical performance of co-electrolysis was much closer to that of H_2O than of CO_2 electrolysis, implying that CO was produced mainly by the chemical reaction between CO_2 and electro-generated H_2 reaction (6).

3.2.3.1. Evidence 1: Gas diffusion and the effect of microstructure. Firstly, the diffusion coefficients of CO_2 were smaller than those for H_2O, with a minor enhancement for CO_2 diffusion by increased binary diffusion coefficients when H_2 was present. However, this positive effect for co-electrolysis would have been valid only for the molecular diffusion regime in larger finger-like voids. Within the sponge-type microstructure close to the electrode | electrolyte interface, Knudsen diffusion would dominate, independently of the gas mixture.

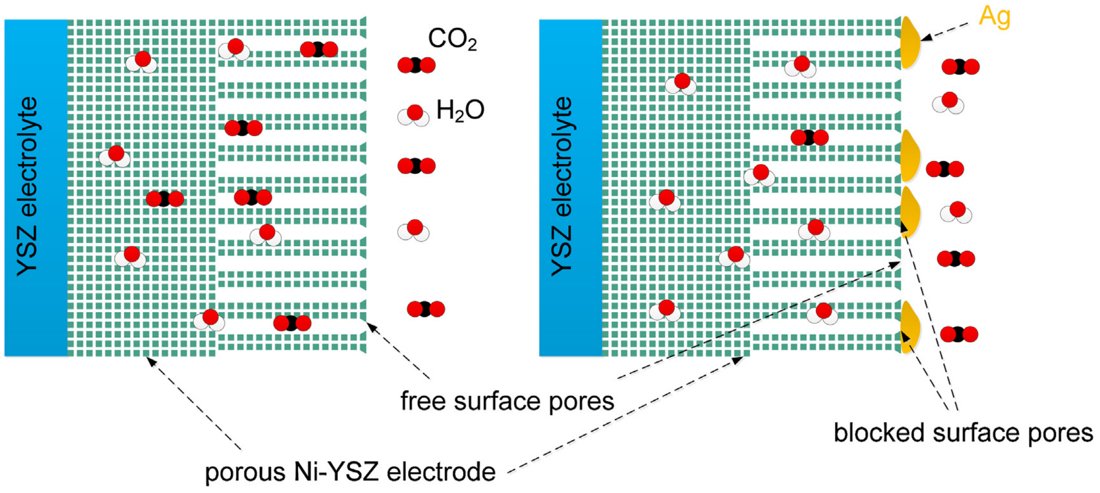

Fig. 8. Schematic of the effect of silver partially blocking entrances to surface pores, so inhibiting CO_2 and H_2O diffusion.

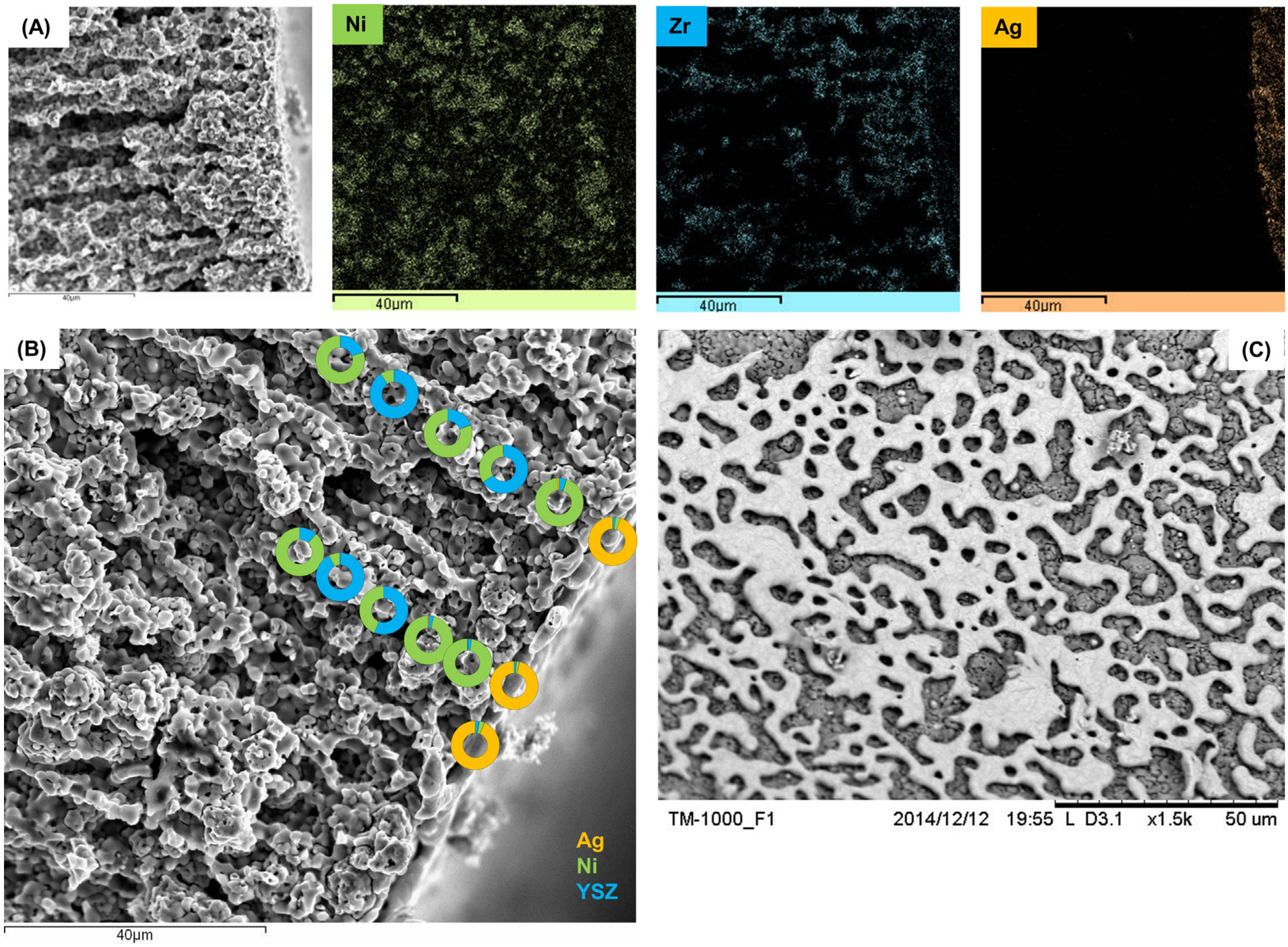

Fig. 9. (A) Elemental mapping of Ni, Zr and Ag; (B) quantitative analysis of individual spots and (C) surface view of inner lumen of hollow fibre reactor. Note: elemental quantification over a larger area within the bulk of the structure confirmed a Ni:YSZ ratio equivalent to a NiO:YSZ ratio prior to reduction of 60:40 wt%.

Table 3
Binary diffusion coefficients for the five feed gas species at 822 °C.

	$He/\times$ $10^{-4}\,m^2\,s^{-1}$	$CO_2/\times$ $10^{-4}\,m^2\,s^{-1}$	$CO/\times$ $10^{-4}\,m^2\,s^{-1}$	$H_2O/\times$ $10^{-4}\,m^2\,s^{-1}$	$H_2/\times$ $10^{-4}\,m^2\,s^{-1}$
He		5.57	6.67	8.17	16.2
CO_2	5.57		1.57	2.05	6.24
CO	6.67	1.57		2.52	7.26
H_2O	8.17	2.05	2.52		8.59
H_2	16.2	6.24	7.26	8.59	

Table 4
Knudsen diffusion coefficients for the five gas species at 822 °C.

	$He/\times$ $10^{-4}\,m^2\,s^{-1}$	$CO_2/\times$ $10^{-4}\,m^2\,s^{-1}$	$CO/\times$ $10^{-4}\,m^2\,s^{-1}$	$H_2O/\times$ $10^{-4}\,m^2\,s^{-1}$	$H_2/\times$ $10^{-4}\,m^2\,s^{-1}$
400 nm pore	3.22	0.969	1.22	1.52	4.55
700 nm pore	5.63	1.70	2.13	2.65	7.96

The anode functional layer thickness for hydrogen oxidation on a Ni-YSZ cermet electrode in a SOFC has been reported to be ca. 20–50 μm in the temperature range 700–1000 °C, depending on parameters such as the precursor particle size of YSZ and NiO [28,29]. As hydrogen oxidation kinetics are faster than steam reduction kinetics and H_2O (or CO_2) diffusion rates are slower than those of H_2 (as outlined in Tables 3 and 4), the effective cathode active functional layer thickness in solid oxide electrolyser mode will have been greater than that in SOFC mode, electronic and ionic conductivities being the same for both operational modes. However, in SOE mode, a significant fraction of triple phase boundaries in the 220 μm thick NiO-YSZ cermet cathode would not have been electrochemically active. A quantitative estimate of that fraction would require modelling [30] beyond the scope of this paper. Furthermore, most of these active triple phase boundaries would be located in the sponge-type porosity at the electrode | electrolyte interface (Knudsen diffusion regime), where CO_2 and CO Knudsen diffusion coefficients were significantly smaller than those of H_2 and H_2O.

As shown schematically in Fig. 10, this electrode functional layer results from the difference between the ionic conductivity of the YSZ electrolyte phase and the electronic conductivity of the nickel electrode phase, causing potentials, overpotentials and hence

---

[1] Note: the silver paste was required for establishing contact between the silver wire and Ni-YSZ electrode, as previous experiments without the paste resulted in very poor contact and noisy electrochemical measurements. The nickel wire has a higher mechanical strength (Young's modulus of 160.9 compared to 46.6 GPa, for nickel and silver respectively [39,38]), so enabled better contact without the addition of conductive paste. Note: similar trends in terms of poor electrode performance were detected for a nickel wire with silver paste, confirming the silver paste as the distinguishing factor.

[2] The yield CO to H_2 ratio did not vary within the accuracy of the mass spectrometry. Obviously, the ratio of H_2/CO to H_2O/CO_2 increased with applied cell potential difference as the overall conversion increased.

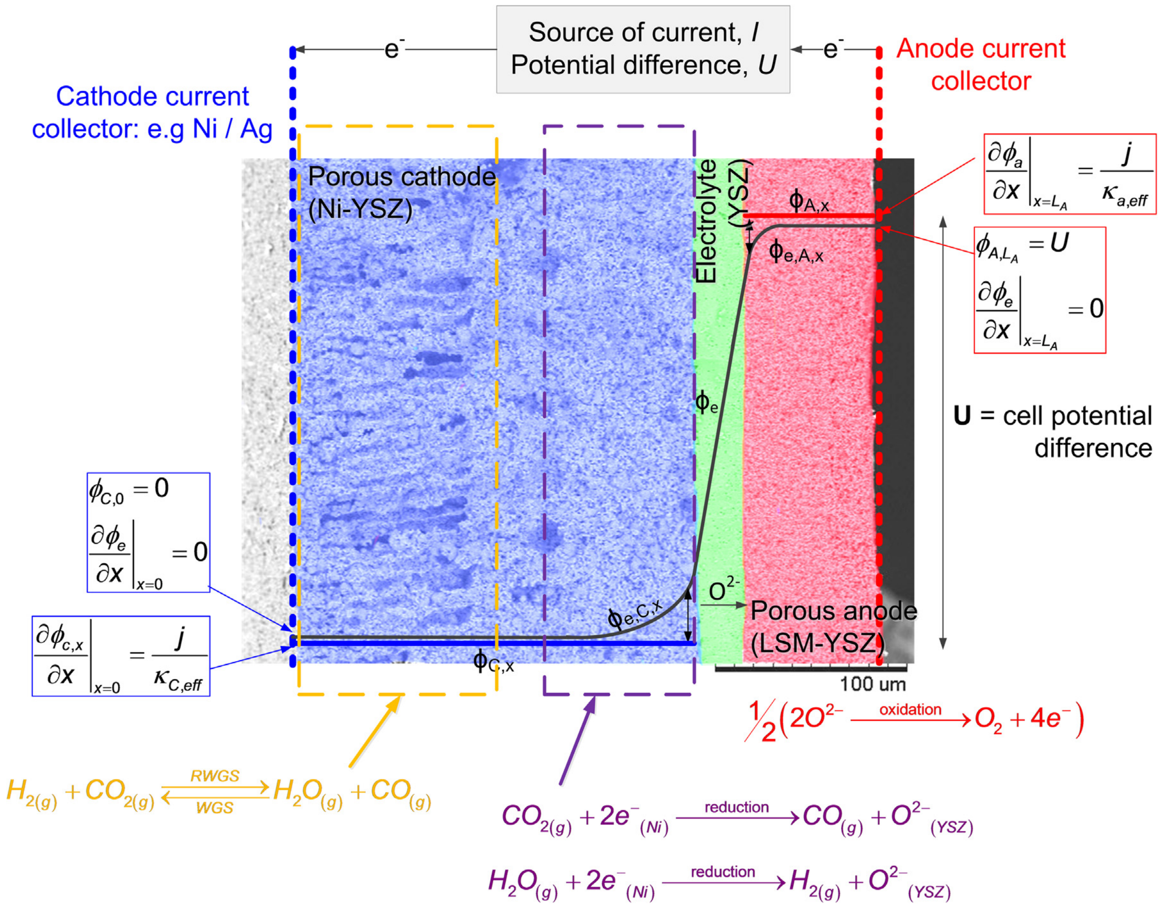

Fig. 10. Schematic of zones in the Ni-YSZ cathode of activity for electrochemical reaction and of heterogeneous catalytic chemical reaction (6), the (reverse) water gas shift reaction.

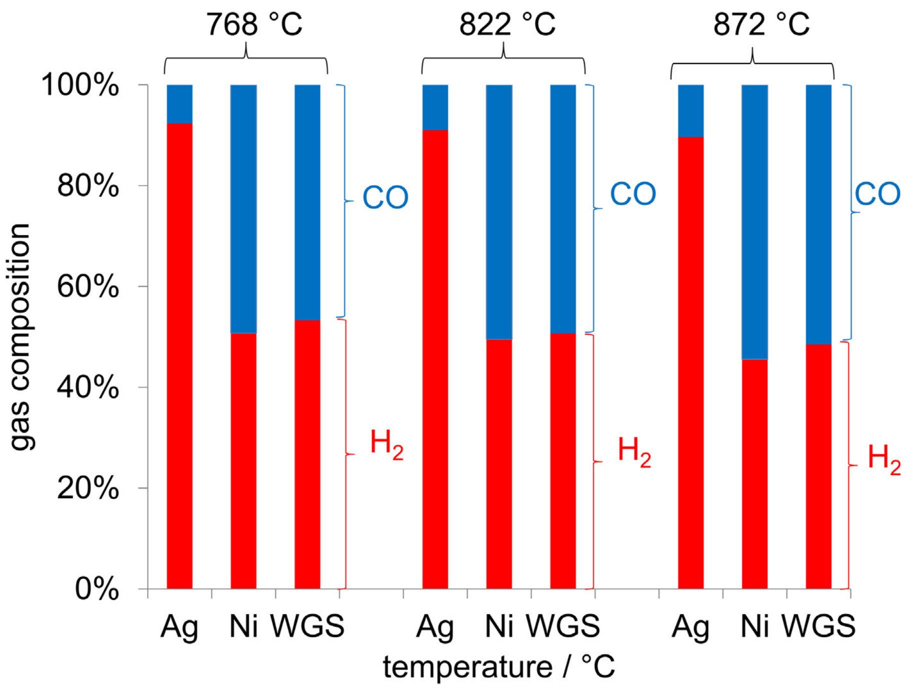

Fig. 11. Effect of temperature on product yield composition for for cathode current collectors containing silver paste and nickel wire only and theoretical yields if the (reverse) water gas shift (WGS) equilibrium was achieved.

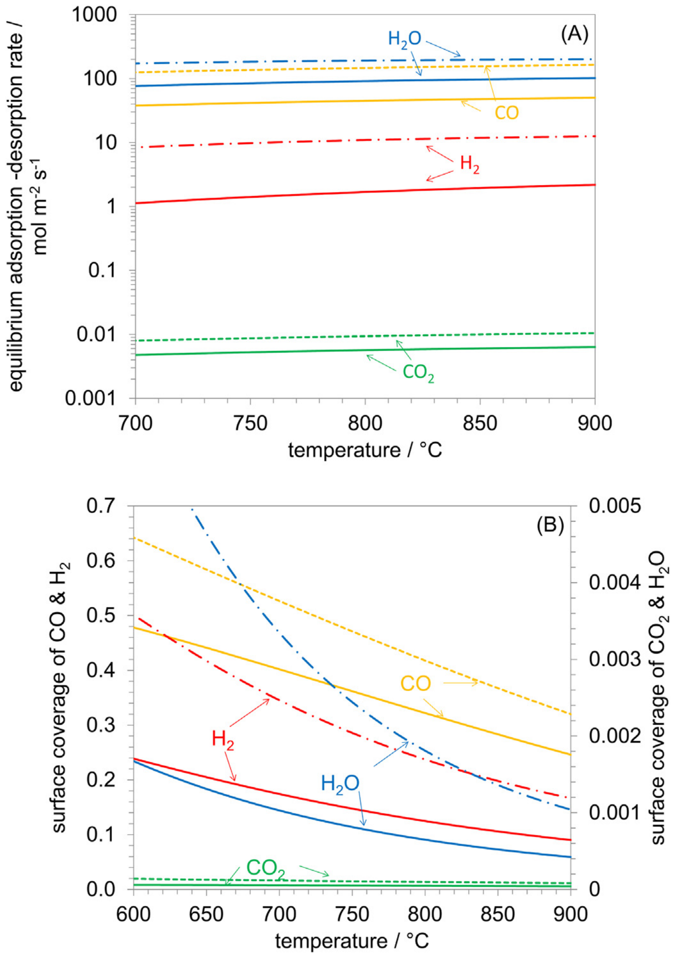

Fig. 12. (A) Equilibrium adsorption rates and (B) surface coverage of H_2O, H_2, CO_2 and CO on Ni for feed gas scenario 1 (- -), 2 (— ·) and 3 (—).

current densities to be spatially distributed in the direction(s) of current flow, with faradaic current densities being concentrated close to the electrode | planar electrolyte interface.

Therefore, the chemical reaction between CO_2 and electro-generated H_2 was probably confined within the finger-type voids (outer 44% of Ni-YSZ), which according to Fig. 10 would have been far less electrochemically active. The reverse water gas shift reaction would have been catalysed by the nickel; i.e. no triple phase boundaries are required, though interactions with the ‘ceramic support’ have been reported to enhance locally rates of the (reverse) water gas shift reaction [31,32]. Thus, a much larger number of active sites for the chemical reaction was provided within the bulk of the Ni-YSZ electrode (Fig. 11), enabling thermodynamic equilibrium for reaction (6) to be achieved.

3.2.3.2. Evidence 2: Gas compositional split of product gases. Fig. 11 shows the product compositional split for (electro-) chemically produced H_2 and CO from on-line mass spectrometric analysis of the cathode off-gases for the two options of current collector design and the theoretical compositional split, if the (reverse) water gas shift equilibrium compositions were achieved. Note that the experiments to quantify outlet gas compositions were run under constant current at ca. 1.3, 1.5 and 1.7 V, but the differences in gas composition of the yield[2] were marginal, so that data in Fig. 11 represent averaged values. Charge yields of ca. 100% were confirmed using Faraday's law.

For the nickel wire cathode current collector, the compositional yield split was ca. 50:50 (temperature dependent), whereas the electrochemical performance was closer to that of H_2O electrolysis than CO_2 electrolysis (80:20 H_2O:CO_2 electrolysis current density). However, the relatively small difference between steam electrolysis and ($CO_2 + H_2O$) co-electrolysis could also have been due to the lower partial pressure of H_2O in co-electrolysis ($p_{H_2O} = 0.18 \times 10^5$ Pa and $p_{CO_2} = 0.18 \times 10^5$ Pa) compared to H_2O electrolysis alone ($p_{H_2O} = 0.36 \times 10^5$ Pa). Thus, the H_2O reactant conversion would have also been twice in co-electrolysis mode, which could have increased reactant polarization.

Furthermore, when silver paste was applied to the current collector of the reactor’s lumen, thermodynamic equilibrium compositions were not achieved, as partial blockage of surface pores hindered CO_2 diffusing into the electrode structure. As the heterogeneously-catalysed water gas shift reaction was fast [33], if CO_2 was present within the Ni-YSZ cathode and penetrated to the electrode functional layer to react electrochemically, thermodynamic equilibrium would have been achieved for the water gas shift reaction (6). Hence, if partial surface blockage could limit the influx of CO_2, diffusional hindrance to reach the electrode functional layer would have been important for all reaction; i.e. the electrochemical reaction was most likely to have been H_2O reduction alone by reaction (1b).

With CO_2 being blocked partially from entering pores, the water gas shift reaction would then have been confined to a decreased number of nickel surface sites, decreasing heterogeneous reaction rates. Homogenous reverse water gas shift reaction within the gas phase has been reported to be slow compared to heterogeneous reaction rates on nickel sites [33,34]; thus, the overall chemical reaction rate would have been smaller with partially blocked surface pore entrances, precluding equilibrium compositions of the reverse water gas shift reaction from being achieved.

Table 5
Parameters used to calculate the adsorption/desorption and surface coverage.

	A (or a)/(m, mol, s)	β (or b)/-	E_a (or d_i)/ kJ mol^{-1}
$H_2 + Ni_{(s)} + Ni_{(s)} \rightarrow H_{(S)} + H_{(S)}$	5.593×10^{15}	0.0	88.12
$H_2O + Ni_{(s)} \rightarrow H_2O_{(s)}$	4.579×10^{12}	0.0	62.68
$CO_2 + Ni_{(s)} \rightarrow CO_{2(s)}$	9.334×10^{7}	0.0	28.80
$CO + Ni_{(s)} \rightarrow CO_{(S)}$	4.041×10^{11}	0.0	112.85
Additional surface coverage dependence of E_a (ε_{CO}):			50.0
$H_{(s)} + H_{(s)} \rightarrow Ni_{(s)} + Ni_{(s)} + H_2$	1×10^{-2}	0.0	0.0
$H_2O_{(s)} \rightarrow Ni_{(s)} + H_2O$	1×10^{-1}	0.0	0.0
$CO_{2(s)} \rightarrow Ni_{(s)} + CO_2$	1×10^{-5}	0.0	0.0
$CO_{(s)} \rightarrow Ni_{(s)} + CO$	5×10^{-1}	0.0	0.0
site occupancy number (σ_k): 1[−]			
surface site density (Γ): 2.60×10^{-5} mol m^{-2}			

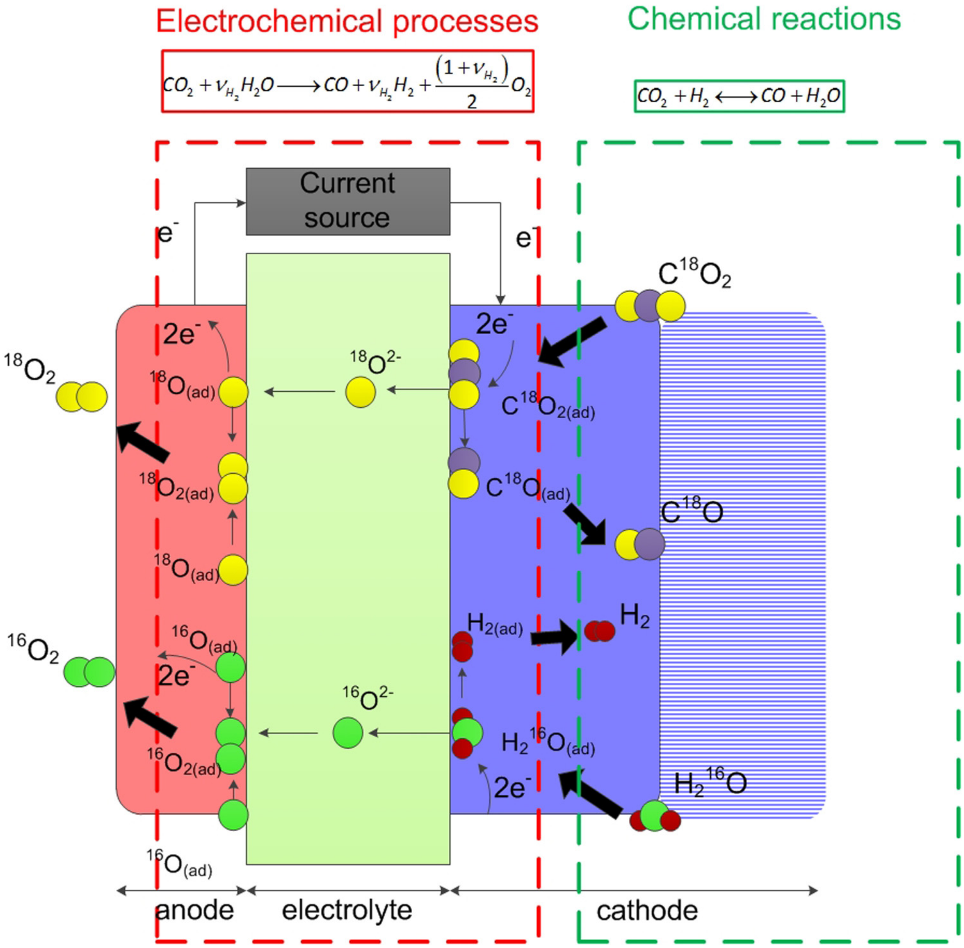

Fig. 13. Schematic of experiment using $C^{18}O_2$ to distinguish between direct electrochemical reduction of CO_2 and its (indirect) chemical with electrochemically-generated H_2 by the reverse water gas shift reaction (6).

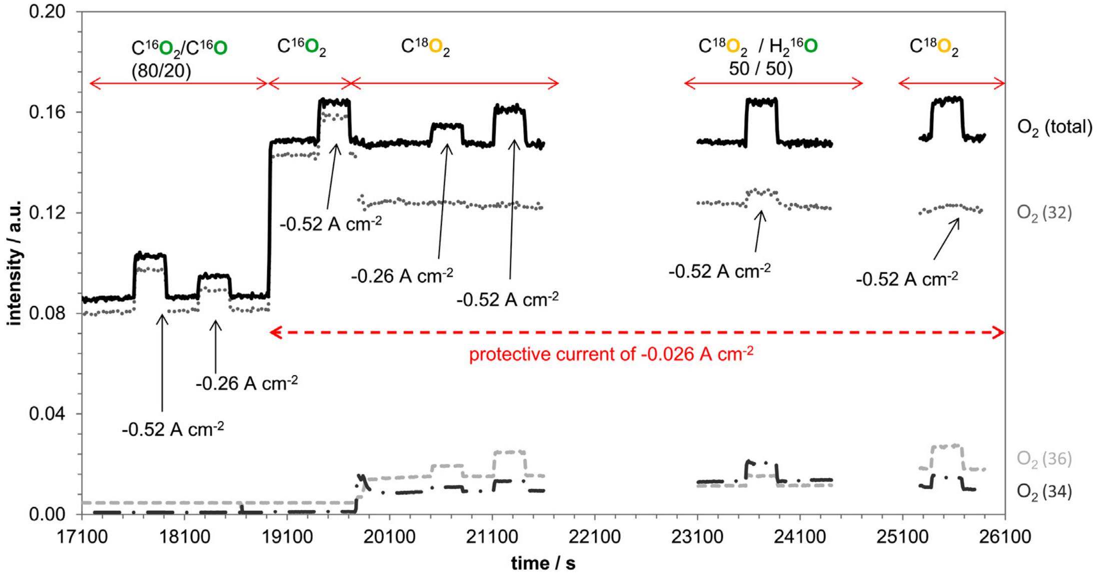

Fig. 14. Mass spectrometric intensities measured at the anode for isotopic oxygen fractions (36–$^{18}O_2$, 34–$^{16}O^{18}O$ and 32–$^{16}O_2$) at different cathodic feed gas compositions and electrolysis current densities at 822° C operating temperature.

Table 6
Oxygen 16 and 18 fractions for different feed gas compositions and current densities at 822 °C.

	Current density/A cm^{-2}	O–16	O–18
$C^{16}O_2/C^{16}O$	–0.52	100%	0%
	–0.26	100%	0%
$C^{16}O_2$ alone	–0.52	100%	0%
$C^{18}O_2$ alone	–0.26	15%	85%
	–0.52	14%	86%
$C^{18}O_2\backslash H_2{}^{16}O$	–0.52	53%	47%
$C^{18}O_2$ alone	–0.52	17%	83%

3.2.3.3. Evidence 3: Gas adsorption. Fig. 12(A) shows the equilibrium adsorption/desorption rates of the four gas feed species in their respective gas feed scenarios[3], and calculated by solving simultaneously the adsorption and desorption Eq. (11)–(17) using data in Table 5 [35,36,37].

$$rate_{ads,i} = k_{a,i}[c_k][c_{Ni\quad sites}]^m \tag{11}$$

$$k_{a,i} = \frac{S_i^0}{(\Gamma_{total})^v}\sqrt{\frac{RT}{2\pi M_i}} \tag{12}$$

$$S_i^0 = a_i T^{b_i} \exp\left(-\frac{d_i}{RT}\right) \tag{13}$$

$$c_{Ni\,sites} = \frac{(1-\sum_{k=1}^{K_s}\theta_k)\Gamma}{\sigma_k} \tag{14}$$

$$rate_{des,i} = k_{d,i}[c_{surf,k}]^v \tag{15}$$

$$k_{d,i} = A_i T^{\beta_i} \exp\left(-\frac{E_{a,i}}{RT}\right)\exp\left(-\frac{\varepsilon_{ki}\theta_k}{RT}\right) \tag{16}$$

$$c_{surf,i} = \frac{\theta_i \cdot \Gamma}{\sigma_i} \tag{17}$$

In co-electrolysis, H_2O adsorption was predicted to be four orders of magnitude faster than CO_2 adsorption. Thus, it seems plausible that steam electrolysis was the dominant electrochemical process, whereby carbon monoxide was produced mainly via the reverse water gas shift reaction (6), especially in view of the additional evidence from gas diffusion and gas compositional changes. Furthermore, with CO responsible for >30 % surface site coverage, blocking active reaction sites (> 41% total coverage in co-electrolysis at 822 °C, compared with 22% total coverage for electrolysis of H_2O alone), the preferred strategy could be to use steam electrolysis followed by indirect CO_2 reduction for syngas production. This would also enable the syngas composition to be tuned better to the requirements of downstream processes.

3.2.4. Labelled $C^{18}O_2$ /$H_2{}^{16}$electrolysis

In order to distinguish further between the relative rates and product distributions of electrochemical versus chemical reactions within the hollow fibre reactors (Fig. 13), the experiments described above were repeated, but with $C^{16}O_2$ replaced by 95.5% oxygen-18 enriched isotopically-labelled $C^{18}O_2$. Both anode and cathode off-gas streams were monitored separately using the same model of mass spectrometer. In order to limit the possibility of the water gas shift reaction exchanging labelled oxygen prior to the reactor, H_2O and CO_2 alone were feed to the reactor at 50:50 molar ratio with a total active gas flow of 40 ml min^{-1}, comparable to gas flow scenario 3 in Table 1, while a cathodic current of –0.026 A cm^{-2} was applied to the cell to protect the nickel from re-oxidation.

Fig. 14 shows an exemplar result of mass spectrometric analyses of the anode off-gases at different operating conditions, highlighting that the labelled oxygen could indeed be distinguished. Assuming that the labelled oxygen signal (32, 34 and 36) intensities would scale similarly regardless of the isotope, the isotopic oxygen fractions from the anode could be calculated (Table 6). Note that using the mass spectrometric analysis of the cathode off-gas, the CO_2 fractions were 83% ($C^{18}O_2$), 15% ($C^{16}O^{18}O$) and 2% ($C^{16}O_2$) %, implying a 90.5% isotopic enrichment in contrast to the 95.5% certified. Thus, the signal intensities were not exactly the same for the different isotopes, but within 5% error. Hence, the data for $C^{18}O_2$ alone in Table 6 were reasonable in comparison to

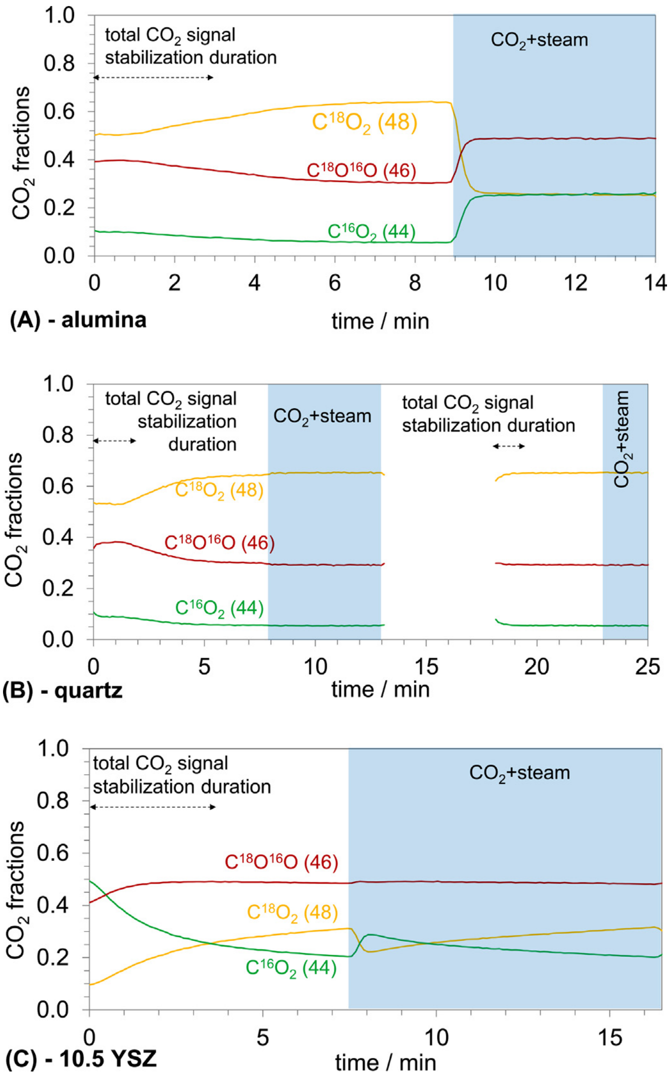

Fig. 15. Effect of thick-walled $^1/_4$ inch OD tube material and introduction of water on CO_2 fractions (44: $C^{16}O_2$, 46: $C^{18}O^{16}O$, 48: $C^{18}O_2$) at 822 °C for (A) alumina, (B) quartz and (C) 10.5 YSZ – Scenario C.

---

[3] Note: the feed gas composition for co-electrolysis (scenario 3), was allowed to reach the (reverse) water gas shift equilibrium composition at the respective temperature. These equilibrium compositions were calculated for reaction (6) using thermodynamic data from [4,5].

the ‘measured’ enrichment, allowing for some back-diffusion of oxygen-16 into the YSZ membrane, as the anode sweep gas contained 10% $^{16}O_2$, and/or residual oxygen-16 within the YSZ membrane. The results for co-electrolysis imply that both CO_2 and H_2O participated equally in the electrochemical process within the error of the isotopic mass spectrometry analysis. However, it was evident from analyses of the cathode off-gases (not shown here), that, unfortunately, the isotopic oxygen labels were being exchanged between CO_2 and H_2O; i.e. oxygen-18 enrichment in the steam and oxygen-16 replacement in the carbon dioxide, so the anode off-gas isotopic fractions were meaningless.

The first cause of the isotopic exchange would be associated with the water gas shift reaction. However, the H_2/CO yields were similar to what has been reported in Fig. 11; i.e. the (reverse) water gas shift (WGS) equilibrium composition was achieved for cells with cathode current collectors of Ni wire alone, whereas cells with the inner lumen of the hollow fibre partially covered in silver paste produced more H_2. Hence, it would appear bizarre if the (reverse) WGS reaction was responsible for exchanging labelled oxygen, but did not reach equilibrium, especially as the ratio of H_2O/CO_2 compared to products (H_2/CO) was in excess of 19:1.

To elucidate the reasons for these observations, the hollow fibre reactor was replaced by an alumina tube and $C^{16}O_2/H_2$ (scenario A), $H_2{}^{16}O/C^{16}O$ (scenario B) and $C^{18}O_2$ and $H_2{}^{16}O$ (scenario C) at different compositions were fed through the alumina tube at the operating temperature of 822 °C. Neither scenario A nor scenario B (Supplementary data: Fig. S1 A–C), representing the left and right hand-side of the reverse water gas shift reaction (reaction 6), respectively, showed any marked variation in the gas composition. Hence, in the absence of nickel catalyst, the homogeneous gas phase (reverse) water gas shift reaction rates were negligible, However, the $C^{18}O_2$ and $H_2{}^{16}O$ (scenario C) exchanged oxygen-16 and oxygen-18 immediately, though the total amount of carbon dioxide and steam remained the same; i.e. any (intermediate) product was unstable (Fig. 15 A).

On repeating this experiment with a quartz tube instead of an alumina tube, no exchange reaction occurred in any of the three scenarios. Hence, it can be concluded that the exchange of labelled oxygen occurred via adsorbed carbon dioxide and water on the alumina. Unfortunately, using a quartz tube in the reactor system was precluded, as the thermal expansion coefficients [38] of alumina and zirconia (ca. 9×10^{-6} compared to $10 \times 10^{-6}\,°C^{-1}$) were better matched than zirconia with quartz (ca. $0.7 \times 10^{-6}\,°C^{-1}$), so sealing was more facile in the former case. Extending this investigation to a thick YSZ tube, resulted in even more O-18 swapped labels, as the oxygen could self-diffuse via vacancies into the lattice as well, replenishing the surface O-16 for further exchange; hence, only a small initial decrease resulted following the introduction of water, as there was another fast process allowing isotope exchange. The results for YSZ indicated a fast surface-exchange of CO_2; a detailed study of the self-diffusion of $^{18}O^{2-}$ ions from $C^{18}O_2$ into YSZ has been reported elsewhere [39].

4. Conclusions

CO_2 and/or H_2O were reduced to CO/H_2 in micro-tubular solid oxide electrolysers with 26 μm thick yttria-stabilized zirconia (YSZ) electrolyte, Ni-YSZ cermet cathode and strontium-doped lanthanum manganite (LSM) oxygen-evolving anode. With a silver wire plus silver paste cathode current collector and a potential difference of 1.5 V, current densities for splitting H_2O alone and CO_2 alone were -0.46 and $-0.24\,A\,cm^{-2}$, respectively. By contrast, with a nickel wire cathode current collector without any paste, current densities increased by 63% to $-0.76\,A\,cm^{-2}$ for H_2O electrolysis at $p_{H2O} = 0.36 \times 10^5$ Pa, but the difference between the performances of H_2O and CO_2 electrolyses decreased to only 16%. SEM images and impedance spectra strongly suggested that silver paste as a component of the cathode current collector caused partial blocking of surface pores in the cathode lumen. This inhibited gas diffusion rates and exacerbated differences in current densities between CO_2 and H_2O electrolyses at fixed potential differences, due to the smaller diffusion coefficient of CO_2 compared to that of H_2O.

Co-electrolysis was found to proceed mainly via the reverse water gas shift reaction between CO_2 and the electro-generated H_2. The supporting evidence included similar electrochemical performances of ($CO_2 + H_2O$) co-electrolysis and H_2O splitting, faster gas diffusion for H_2O, the reactor microstructure, compositional off-gas analysis and adsorption/desorption modelling of reactant and product gases onto cathode materials.

Unfortunately, when isotopically-labelled $C^{18}O_2$ was used in an attempt to further confirm this hypothesis, isotopic oxygen labels were exchanged between $C^{18}O_2$ and $H_2{}^{16}O$, enriching oxygen-18 in the steam and substituting oxygen-16 into the carbon dioxide, so the anode off-gas isotopic fractions were meaningless. This occurred even in alumina or YSZ tubes without the micro-tubular reactor, i.e. even without a Ni catalyst, though not in a quartz tube. However, mismatched thermal expansion coefficients of quartz with the micro-tubular reactors precluded its use as a feed-tube material. However, valuable insight into the behaviour of CO_2 on ceramic materials was obtained, including fast surface-exchange of CO_2 in YSZ.

Acknowledgements

The authors gratefully acknowledge the Engineering and Physical Science Research Council (EPSRC) for funding studentships for L.K. (Grant: EP/K035274/1) and T.L. (Grant: EP/G012679/1).

Appendix A. Supplementary data

Supplementary data associated with this article can be found, in the online version, at http://dx.doi.org/10.1016/j.electacta.2015.07.062.

References

[1] R.M. Ormerod, Solid oxide fuel cells, Chem. Soc. Rev. 32 (1) (2003) 17–28.

[2] K. Eguchi, H. Kojo, T. Takeguchi, R. Kikuchi, K. Sasaki, Fuel flexibility in power generation by solid oxide fuel cells, Solid State Ionics 152–153 (2002) 411–416.

[3] S.D. Ebbesen, M. Mogensen, Electrolysis of carbon dioxide in Solid Oxide Electrolysis Cells, J. Power Sources, vol 193 (2009) 349–358 1.

[4] M. W. Chase, NIST-JANAF Thermochemical Tables, Fourth Edition, J. Phys. Chem. Ref. Data, vol. Monograph No. 9, pp.1–1951, 1998.

[5] E.F.G. Herington, Recommended reference materials for the realization of physicochemical properties, Pure Appl. Chem. 40 (3) (1974) 391–472.

[6] C.M. Stoots, J.E. O'Brien, J.S. Herring, J.J. Hartvigsen, Syngas Production via High-Temperature Coelectrolysis of Steam and Carbon Dioxide, J. Fuel Cell Sci. Technol. 6 (1) (2008) 11014.

[7] W.L. Becker, R.J. Braun, M. Penev, M. Melaina, Production of Fischer-Tropsch liquid fuels from high temperature solid oxide co-electrolysis units, Energy 47 (1) (2012) 99–115.

[8] L. Chen, F. Chen, C. Xia, Direct synthesis of methane from CO_2-H_2O co-electrolysis cells, Energy Enivron. Sci. vol. 7 (no. 12) (2014) 4018–4022.

[9] X. Yue, J.T.S. Irvine, (La,Sr)(Cr,Mn)O_3/GDC cathode for high temperature steam electrolysis and steam-carbon dioxide co-electrolysis, Solid State Ionics 225 (2012) 131–135.

[10] P. Kim-Lohsoontorn, J. Bae, Electrochemical performance of solid oxide electrolysis cell electrodes under high-temperature coelectrolysis of steam and carbon dioxide, J. Power Sources 196 (17) (2011) 7161–7168.

[11] C.J. Moyer, N.P. Sullivan, H. Zhu, R.J. Kee, Polarization Characteristics and Chemistry in Reversible Tubular Solid-Oxide Cells Operating on Mixtures of H_2, CO, H_2O, and CO_2, J. Electrochem. Soc. 158 (2) (2011) B117–B131.

[12] Z. Zhan, W. Kobsiriphat, J.R. Wilson, M. Pillai, I. Kim, S.A. Barnett, Syngas Production By Coelectrolysis of CO_2/H_2O: The Basis for a Renewable Energy Cycle, Energy Fuels 23 (6) (2009) 3089–3096.

[13] Y. Matsuzaki, I. Yasuda, Electrochemical Oxidation of H_2 and CO in a H_2-H_2O-CO-CO_2 System at the Interface of a Ni-YSZ Cermet Electrode and YSZ Electrolyte, Electrochem. Soc. 147 (5) (2000) 1630–1635.

[14] Z. Zhan, L. Zhao, Electrochemical reduction of CO_2 in solid oxide electrolysis cells, J. Power Sources, vol 195 (21) (2010) 7250–7254.

[15] S.D. Ebbesen, C. Graves, M. Mogensen, Production of Synthetic Fuels by Co-Electrolysis of Steam and Carbon Dioxide, Int. J. Green Energy 6 (6) (2009) 646–660.

[16] M. Ni, 2D thermal modeling of a solid oxide electrolzer cell (SOEC) for syngas production by H_2O/CO_2 co-electrolysis, Int. J. Hydrogen Energy 37 (8) (2012) 6389–6399.

[17] L. Kleiminger, T. Li, K. Li, G.H. Kelsall, CO_2 splitting into CO and O_2 in micro-tubular solid oxide electrolysers, RSC Adv. 4 (91) (2014) 50003–50016.

[18] X. Meng, X. Gong, Y. Yin, N.-T. Yang, X. Tan, Z.-F. Ma, Microstructure tailoring of YSZ/Ni-YSZ dual-layer hollow fibers for micro-tubular solid oxide fuel cell application, Int. J. Hydrogen Energy 38 (16) (2013) 6780–6788.

[19] X. Tan, Y. Liu, K. Li, Mixed conducting ceramic hollow-fiber membranes for air separation, AIChE J. 51 (7) (2005) 1991–2000.

[20] R.A. Matula, Electrical Resistivity of Copper, Gold, Palladium, and Silver, J. Phys. Chem. Ref. Data 8 (4) (1979) 1147–1199.

[21] M. Yousuf, P.C. Sahu, K.G. Rajan, High-pressure and high-temperature electrical resisitivity of ferromagnetic transition metals: Nickel and iron, Phys. Rev. B 34 (11) (1986) 8086–8100.

[22] L. Kleiminger, T. Li, K. Li, G.H. Kelsall, Effects of Current Collector Materials on Performances of Micro-Tubular Solid Oxide Electrolysers for Splitting CO_2, ECS Trans. 68 (1) (2015) 3449–3458.

[23] C. Yang, C. Jin, F. Chen, Performances of micro-tubular solid oxide cell with novel asymmetric porous hydrogen electrode, Electrochim. Acta 56 (1) (2010) 80–84.

[24] E.-C. Shin, P.-A. Ahn, H.-H. Seo, J.-M. Jo, S.-D. Kim, S.-K. Woo, J.H. Yu, J. Mizusaki and J.-S. Kee, Polarization mechanism of high temperature electrolysis in a Ni-YSZ/YSZ/LSM solid oxide cell by parametric impedance analysis, Solid State Ionics 232 (2013) 80–96.

[25] Y. Matteucci, B.D. Freeman, I. Pinnau, Transport of Gases and Vapors in Glassy and Rubbery Polymers, in: Y. Yampolskii, I. Pinnau, B.D. Freeman (Eds.), Materials Science of Membranes for Gas and Vapor Separation, Wiley, Chichester, UK, 2006, pp. 6.

[26] E.N. Fuller, P.D. Schettler, J.C. Giddings, New method for prediction of binary gas-phase diffusion coefficients, Ind. Eng. Chem. 58 (5) (1966) 18–27.

[27] U. Doraswami, Modelling of Micro-Tubular Hollow Fibre Solid Oxide Fuel Cells, Ph.D. Thesis, Imperial College London, London, UK, 2010.

[28] S. Primdahl, M. Mogensen, Oxidation on Hydrogen on Ni/Yttria-Stabilized Zirconia Cermet Anodes, J. Electrochem. Soc. 144 (10) (1997) 3409–3419.

[29] K. J. Kong, D. Sun, N. Zhou, J. Mu Zhang, Ni-YSZ gradient anodes for anode-supported SOFCs, J. Power Sources 166 (2) (2007) 337–342.

[30] U. Doraswami, N. Droushiotis, G.H. Kelsall, Modelling effects of current distributions on performance of micro-tubular hollow fibre solid oxide fuel cells, Electrochim. Acta 55 (2010) 3766–3778.

[31] R. Burch, Gold catalysts for pure hydrogen production in the water-gas shift reaction: activity, structure and reaction mechaism, Phys. Chem. Chem. Phys. 8 (47) (2006) 5483–5500.

[32] L. Wang, S. Zhang, Y. Liu, Reverse water gas shift reaction over Co-precipitated Ni-CeO_2 catalysts, J. Rare Earth., vol 26 (1) (2008) 66–70.

[33] W. Lehnert, J. Meusinger, F. Thom, Modelling of gas transport phenomena in SOFC anodes, J. Power Sources 87 (1–2) (2000) 57–63.

[34] F. Bustamante, R.M. Enick, A.V. Cugini, R.P. Killmeyer, B.H. Howard, K.S. Rothenberger, M.V. Ciocco, B.D. Morreale, S. Chattopadhyay, S. Shi, High-Temperature Kinetics of the Homogeneous Reverse Water-Gas Shift Reaction, AIChE J. 50 (5) (2004) 1028–1041.

[35] C. Li, Y. Shi, N. Cai, Elementary reaction kinetic model of an anode-supported solid oxide fuel cell fueled with syngas, J. Power Sources 195 (8) (2010) 2266–2282.

[36] R.J. Kee, M.E. Coltrin, P. Glarborg, Chemically reacting fow: theory and practice, USA: Wiley, New York, 2003445–486.

[37] L. Maier, R., Schwiedernoch, B. Schaedel and O. Deutschmann, CH4 on Ni - Surface mechanism, 21/1/2005. [Online]. Available: http://www.detchem.com/mechanisms/sm_Ni_CH4_H2O_CO2_O2_1.0_DETCHEM [Accessed 21/04/2015].

[38] F. Ashby, Materials Selection in Mechanical Design, Butterworth-Heinemann, Burlington, USA, 201083.

[39] L. Kleiminger, PhD Thesis: Solid oxide electrochemical reactors and processes for carbon dioxide and water splitting, Imperial College London, London, UK, 2015.